# Development of a Stiffness-Adjustable Articulated Paddle and its Application to a Swimming Robot

*Bokeon Kwak, Soyoung Choi, and Joonbum Bae**

**Stiffness of a swimming appendage is the key mediator between thrust generated and its beating frequency. Due to the advantageous role of flexible propulsors, they are widely adopted in previous swimming robots. As an optimal propulsor, stiffness is highly dependent on its beating frequency, and stiffness modulation is crucial when a robot is swimming with multiple beating frequencies. Herein, a novel swimming paddle that can switch two different stiffness states by sliding a laminate inside and its application to a swimming robot is studied. This paddle has 8 articulated joints and 20 passive flaps to achieve drag asymmetry with minimum control effort. A semiempirical model to estimate the stiffness change in good accuracy is also studied. The thrust modulation caused by stiffness change is comprehensively studied by varying frequency and range of motion. In addition, a nontethered swimming robot propelled by a bilateral pair of paddles is developed to investigate when and how the stiffness adjustment is useful. There is a threshold frequency dividing two regimes where one stiffness excels the other stiffness with respect to cost of transport. Finally, it is shown that the paddle thickness is closely related to the necessity of stiffness change mechanism.**

## 1. Introduction

Flexible propulsors of animals are universal in nature owing to their hydrodynamic efficiency.[1] Deformation of a flexible propulsor was advantageous over a rigid propulsor in thrust enhancement owing to directed fluid flow toward a preferential axis without much loss.[2] The advantage of a flexible flipper over a rigid flipper was recently demonstrated using an underwater vehicle system.[3] Besides employing a flexible propulsor, the degree of flexibility significantly affects in thrust and propulsion efficiency.[4–6] For example, an optimal beating frequency, which yielded the highest efficiency and thrust, was varied depending on the flexibility of propulsors.[4,5] A fixed but universally optimal stiffness in varying beating frequencies was indeed not found from previously developed swimming appendages.[7–9] In the case of fish robots, an optimal driving frequency to achieve the fastest swimming speed was also different when the flexibility of a pectoral fin or a body was changed.[10,11] For some flexible propulsors, such optimal frequency was sometimes related with resonance.[6] The critical effect of flexibility in hydrodynamic propulsion have motivated the developments of various propulsive surfaces and swimming robots with stiffness-adjustable abilities.

Three pairs of bilaterally aligned ICPF (ionic conducing polymer gel film) actuators were used in ref. [12] to mimic the ciliary movement of a paramecium by adjusting the actuator stiffness. The intrinsic stiffness of ICPF actuator was tunable with low power, but the thrust output was small (less than 1 mN). The same group also applied a variable effective-length spring and torsional rectangular plates to study a stiffness-adjustable fin.[13,14] Both of these works could generate much larger thrust than the ICPF actuator and adjust the stiffness by changing the fin shape. More importantly, both mechanisms exhibited enhancement of thrust upon increasing the stiffness and fin beating frequency. The same trend was also reported from other swimming robots,[8,10,11,15] but without employing an active stiffness-adjustable mechanism. An endoskeleton that composed of serially connected rigid and soft elements was utilized to implement a tendon-driven variable stiffness mechanism,[16] and its application to a robotic dolphin was studied in ref. [17]. These works again showed a positive correlation between optimal stiffness of fin and its beating frequency.

If a swimming robot has multiple stiffness-adjustable joints, their distribution also affect swimming performance. Multiple electric motors were controlled as virtual rotational springs to optimize the stiffness distribution of a multi-segmented swimming robot in ref. [18]. From series of online optimization, it was found that having different stiffness among the joints outperformed a uniform stiffness distribution in terms of thrust. Similar aspect has been addressed in ref. [11] using a tensegrity fish robot. Although this robot could not actively change its tail stiffness, the importance of stiffness distribution was shown to have huge impact in swimming speed. Both uniform and uniform stiffness distribution achieved identical swimming performance; however, a nonuniform distribution can still provide more options that match a target swimming speed.

---

B. Kwak, S. Choi, J. Bae
Bio-Robotics and Control (BiRC) Laboratory
Department of Mechanical Engineering
UNIST
Ulsan 44919, Korea
E-mail: jbbae@unist.ac.kr

The ORCID identification number(s) for the author(s) of this article can be found under https://doi.org/10.1002/aisy.202200348.

**DOI: 10.1002/aisy.202200348**

Stiffness change was also beneficial to perform multiple modes of locomotion (sometimes in different envrionemnt). For example, an amphibious hexapod robot in ref. [19] could traverse on a ground and swim in aquatic environment by adjusting the leg stiffness. A one degree-of-freedom fish robot, which utilized a foil insertion mechanism to change its fin stiffness, was able to show fundamental swimming maneuvers including turning and diving.[20] Recently, buckling was utilized in reconfigurable flexural joints.[21–23] By adjusting the effective length of a curved beam (thereby changing the stiffness), a swimming robot that can switch between rowing and flapping was demonstrated in ref. [21,22]. More improved reconfigurability was shown by vacuuming a soft tube to induce tube-pinching by buckling.[23] By adjusting the negative pressure inside the tube, a variable stiffness torsional spring-like functionality was demonstrated. Also, the location of joint axes can be adjusted using a rigid sleeve. This reconfigurability was useful to show traveling wave for a two-joint linkage robot to swim. However, these buckling based joints exhibited nonlinear hysteresis upon bending and unloading.[21–23] A sliding laminate mechanism could adjust the stiffness of a flexural joint by displacing a thin laminate kept insides that joint.[24] An underwater flapping tail using this mechanism was built, and its stiffness state had a huge effect when swimming in open water and confined channel.

Many stiffness-adjustable propulsors have already been developed as discussed above. However, aquatic rowing shown in **Figure 1** by stiffness-adjustable bilateral propulsors has not been studied widely. Moreover, a rowing propulsor requires different design requirements compared to fish tail-like propolsors. First of all, the hydrodynamic drag produced by flexible propulsors during the power stroke (phase 1–3 in Figure 1) must be greater than that of recovery stroke (phase 4–6 in Figure 1) for forward propulsion. This drag asymmetry can be induced by employing flexible propulsors, which are compliant in posterior side (i.e., opposite of intended swimming direction) but remained stiff in anterior side. The posterior-side compliance is essential to reduce the resistive force during recovery stroke by decreasing the effective area. Whereas, inhibiting the anterior side deformation is required during power stroke to maintain large surface areas of the propulsors. Although this drag-powered rowing was studied in many previous works,[8,10,12,21,22,25–30] only handful of robots had employed stiffness-adjustable propulsors in aquatic rowing.[12,21,22] Due to the tethered power cables, however, the robot was unable to perform free swimming in underwater.[12] Furthermore, the thrust obtained by the actuator was less than 1 mN, which was not enough to propel a fully onboard non-tethered swimming robot. The asymmetric buckling of a curved beam is one way of implementing the rowing motion with symmetric motor input by only allowing the buckling during recovery stroke.[21,22] However, the drag applied to the curved beam must exceed a certain load limit to induce buckling and effectively reduce the drag. This property can potentially limit the operation of a swimming robot driven by a low frequency motor input. Instead, the asymmetric bending of a flexural joint was implemented by a thin film joint and a mechanical stopper, which was similar to ref. [8]. Furthermore, the stiffness of flexural joint was adjusted by adopting the sliding laminate-based approach[24] owing to ease of integration with a film joint-based mechanism. So far, no previous aquatic rowing robots driven by stiffness-adjustable propulsors had demonstrated both enhancement of swimming speed and efficiency upon active stiffness change. Of course, some previous dolphin and fish-inspired robots had already shown a similar result using tail fin propulsors;[11,15,17,31] however, the design requirement for a rowing propulsor is different as mentioned above. Therefore, a new stiffness-adjustable propulsor for rowing needs to be developed and the resultant swimming performance should be verified. In this work, an aquatic rowing robot propelled by novel bilateral stiffness-adjustable propulsors is developed, and in-depth locomotion analysis with respect to range of motion, rowing frequency, and stiffness are investigated.

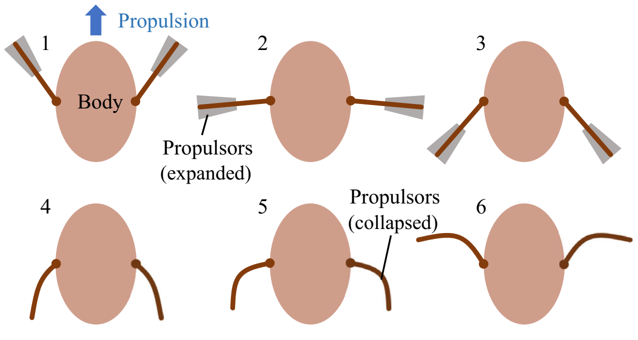

**Figure 1.** The sequence of rowing with a pair of bilateral flexible propulsors (1-3: power stroke, 4-6: recovery stroke). The area of propulsors were enlarged during the power stroke to generate a large thrust followed by the surface area collapse during the recovery stroke for drag reduction.

The contributions of this article are summarized as follows. First, a novel stiffness-adjustable paddle cascaded with dozens of passive flaps for aquatic rowing is developed. Although three main components of the proposed paddle 1) sliding laminate-based variable stiffness,[24,32] 2) film flexural joint with mechanical stopper;[8] and 3) passive flap for extra drag reduction during recovery stroke)[25,26,29] were already addressed from previous studies, this article newly introduced the fabrication method of integrating all these components into a monolithic structure. Secondly, a non-tethered swimming robot propelled by a bilateral pair of paddles is developed to demonstrate the advantage of stiffness change in frequency-varying swimming. The observation of a threshold frequency, which divided energy efficient swimming regime depending on the paddle stiffness, is also addressed. It is also experimentally demonstrated that the proposed paddle enabled a rowing robot to achieve enhancement of both swimming speed and energy efficiency (in terms of cost of transport) upon *active* stiffness change. In our best understanding, no previously developed *rowing* robots had demonstrated anything similar.

The remainder of this article is organized as follows. In Section 2, a new stiffness-adjustable swimming paddle cascaded with passive flaps is designed including a simple model to estimate the stiffness change. The hydrodynamic characteristics of the proposed paddle such as thrust and efficiency is comprehensively analyzed in Section 3. By applying a pair of the proposed paddles to a robotic system in Section 4, the resultant locomotion is also analyzed by focusing on the effect of stiffness change in swimming speed and efficiency. Finally, conclusion and future work is addressed in Section 5.

## 2. Stiffness-Adjustable Swimming Paddle

### 2.1. Selection of Variable Stiffness Mechanism

Many variable stiffness mechanisms were already developed and exhibited different characteristics in terms of physical stimuli, stiffness-change range, reaction time, and power consumption.[33] By considering that working environment of the paddle is underwater and its intended application to non-tethered swimming robot, at least 3 requirements should be met. First, underwater operation should be guaranteed with low risk of failure. Secondly, any auxiliary device required for stiffness change should be small to be contained inside a hull of robot. Therefore, high voltage-based mechanisms (e.g., ER fluid,[34] electrostatic chucking,[35] electro-active polymer)[36] and pneumatic-based mechanism (e.g., a balloon actuator,[37] vacuum induced tube pinching)[23] was not considered because of safety concern and increased complexity by pneumatic hardware, respectively. In the case of using MR (magnetorheological) fluid-based stiffness change,[38] an external device to generate controllable magnetic field is required. Therefore, it was not suitable for a non-tethered robotic application. The third requirement was low power usage to maintain current stiffness state. As a non-tethered robot has limited battery capacity, thermal-based variable stiffness materials such as low melting point alloy (LMPA),[39] shape memory polymer (SMP),[40] conductive propylene elastomer (CPE),[41] and shape memory alloy (SMA)[42] were not considered by considering their large power consumption.

Unlike aforementioned mechanisms, however, a sliding laminate-based method studied in ref. [24,32] meets all the 3 requirements. As illustrated in **Figure 2**a, it can simply change its stiffness by sliding a flexible sheet laminated with rigid elements to offset the alignment state with the opposite layer. Stiffness of all the flexural joints (i.e., rigid element-free area in Figure 2a) were changed in parallel, and no power is needed to maintain stiffness state except displacing the sliding laminate. Although almost the same method was previously introduced as foil-insertion mechanism,[20] we refer the stiffness change method used in this work as sliding laminate, as a multilayered laminate was used indeed. Tendon-driven variable stiffness mechanisms such as an endoskeleton-inspired structure[16] and origami structural element[43] are promising alternatives too. However, this method involved noticeable dimensional change of the structure itself when pulling the tendon for stiffness change. Variable effective-length spring method also exhibited the same dimensional change issue when adjusting its stiffness.[13] On the other hand, sliding laminate-based method does not involve dimensional change (see **Figure 3**), which is advantageous to conduct more consistent experiment. It is also more easier to integrate passive flaps (refer Figure 2b,c), which can reduce negative drag during recovery stroke, than the torsional plate-based variable stiffness (TPVS) mechanism;[14] although TPVS didn't much involve dimensional change during stiffness adjustment, the presence of long plates inside a fin would make difficult to integrate passive structure such as a flap in this case.

### 2.2. Design and Working Principle

The proposed paddle is shown in Figure 2b, which was composed of a trapezoidal substrate paddle (SP in Figure 2c) and

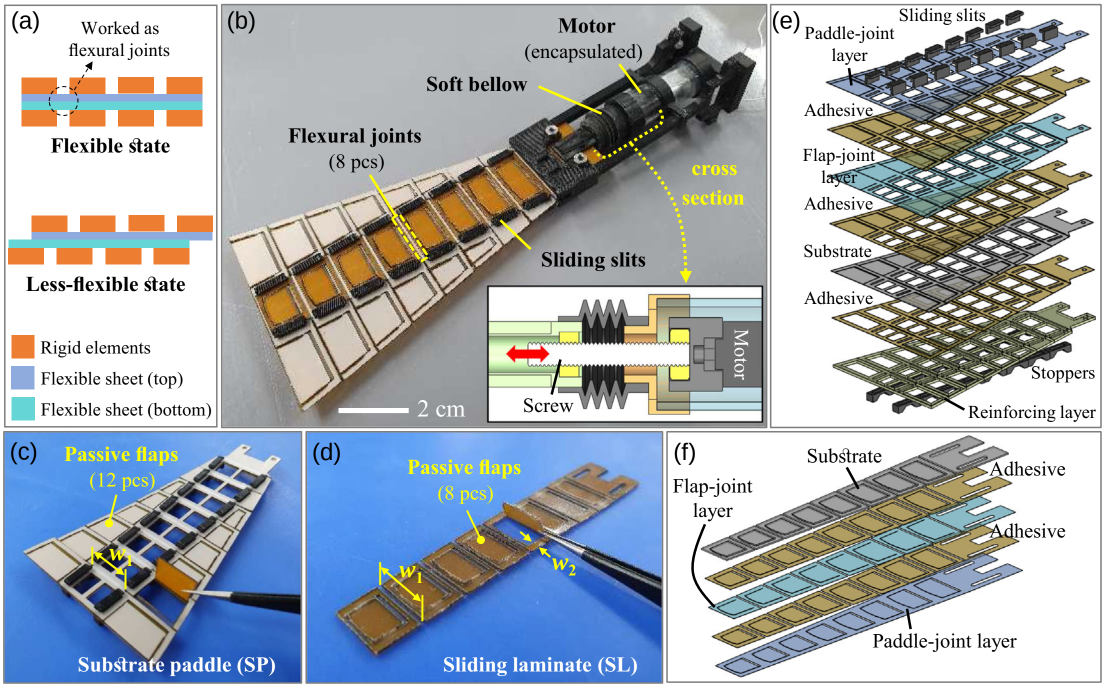

**Figure 2.** The structure of proposed stiffness-adjustable paddle. a): adjustment of bending stiffness by sliding a laminate. b): outline of the proposed paddle. c): a substrate paddle (SP) cascaded with passive flaps. d): a sliding laminate (SL) cascaded with passive flaps. e): exploded view of SP. f): exploded view of SL.

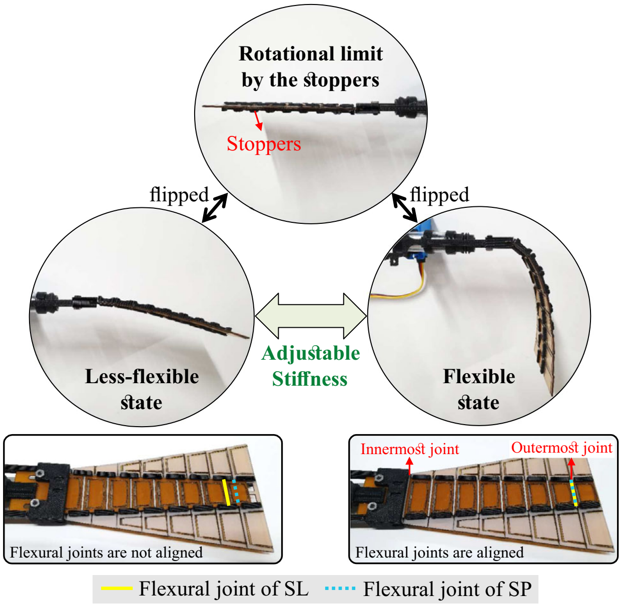

**Figure 3.** Stiffness adjustment of the proposed paddle by moving SL. Alignment of all the flexural joints can maintain the paddle stiffness at flexible state (F-state). Whereas, the joint anti-alignment increased the paddle stiffness and switched to less-flexible state (LF-state).

a sliding laminate (SL in Figure 2d). Inspired by the highly articulated hind legs of a water beetle, which utilizes the same swimming principle shown in Figure 1,[44] both SP and SL had eight flexural joints. This design can also facilitate drag reduction during recovery stroke by passively reduce the effective surface area seen from the swimming direction. As illustrated in Figure 2a, some parts of the flexible sheet free of the rigid elements can be functioned as flexural joints; rest of the areas laminated with the rigid elements are served as rigid links. The width of the flexural joints ($w_1$) were gradually decreased from the innermost joint toward the outermost joint to withstand large force during propulsion. This design was also similar to a low aspect ratio flapping foil of some fishes, which was known to be advantageous for thrust maximization in sprinting.[45] Another key characteristics of the paddle was twenty passive flaps to further reduce the drag during recovery stroke; 12 pieces and 8 pieces were integrated onto SP and SL, respectively (Figure 2c,d). Although such passive flap was already proposed in ref., [25,26,29] the integrated design of passive flaps, flexural joints, and sliding-based variable stiffness mechanism into a single paddle was firstly proposed in this work. The functionality of flexural joints and passive flaps are explored in Section 3.1.

SP was fabricated by laminating 7 layers of laser-cut sheets and 3D printed components such as sliding slits and mechanical stoppers as shown in Figure 2e. The material of the paddle-joint layer and flap-joint layer was 50 μm thick PET (polyethylene terephthalate) film and 12.5 μm thick PI (polyimide) film, respectively. Note that exactly the same materials were used to the flap-joint and paddle-joint layers of SL (Figure 2f). A 0.15 mm thick e-glass was used to the substrate layer of SP; while three different substrate layers (0.2, 0.3, and 0.4 mm thick e-glass) were considered in SL to study various stiffness states (in Section 3 and 4). As it will be shown later, the thickness of substrate layer of SL was influential on stiffness change. SP was additionally laminated with a 0.8 mm thick polycarbonate as a reinforcing layer. This significantly increased the stiffness of rigid areas that supposed not to be bent during propulsion. SP also had stoppers to block one side of bending and to maintain a fully extended paddle during power stroke. Additionally, sliding slits (refer Figure 2b) were adhered on the top surface to provide a constrained track for the translational motion of SL. A small DC geared motor was connected to SL via a screw as shown in the inset of Figure 2b. This screw could move SL and change the paddle stiffness. Compared to electromagnetic actuation of a sliding layer in [46], the stiffness of multiple joints can be adjusted at once using a single motor. This motor was encapsulated inside a plastic tube for waterproof, and a 3D-printed soft bellow was installed between the plastic tube and SL. More detail explanation of manufacturing SP and SL can be found in Note S1, Supporting Information.

The stiffness adjustment mechanism is illustrated in Figure 3. Displacement of SL driven by the DC motor induced stiffness change as intended (Video S1, Supporting Information). At initial state, all the flexural joints of SP and SL were mutually aligned, which maintained a flexible state (i.e., F-state) along the entire paddle. However, those two flexural joint layers were no longer aligned when SL was pulled 5 mm backward. At this stage, the flexural joint area of SP is now faced with the rigid area of SL, which increased the paddle stiffness consequently (i.e., less flexible state; LF-state). Owing to the high gear ratio of the DC motor, SL was not easily displaced unless directly driven by the DC motor. This characteristic enabled the paddle to maintain current stiffness state without power consumption.

### 2.3. Modeling of Flexural Joint Stiffness

To characterize the stiffness change of flexural joint, a theoretical model to estimate the joint stiffness and the corresponding experimental measurements were compared. As the paddle was essentially a chained-like structure interconnected with 8 flexible joints in similar scale, only the stiffness changes of the innermost and outermost joints were investigated as representatives. This allowed us to focus the stiffness change of flexural joint by SL without considering any effect caused by interconnected joints and eased the associated analysis. Illustrations of the flexural joint in two opposite stiffness states are depicted in **Figure 4**a where the joint was bent $\theta$ degrees. Two flexural joint layers ($t_f = 50, 100\,\mu m$) of SP and SL, and three e-glass layers of SL ($t_e = 0.2, 0.3, 0.4$ mm) were considered to investigate broader material combinations. Note that passive flaps were deliberately omitted to better illustrate the bending of e-glass layer in LF-state. Also, the length between the two edges of the sliding slits was denoted as $l_2$ where semi-rigid connections, which will be explained soon, were assumed between the sliding slit and SL. Only the two flexural joint layers were bent at F-state; whereas, the flexural joint layer of SP and the rigid part of SL (i.e., non-flexural-joint area) were bent in LF-state. Young's moduli of each materials except the reinforcing layer were summarized in **Table 1**. As the purpose of reinforcing layer was to

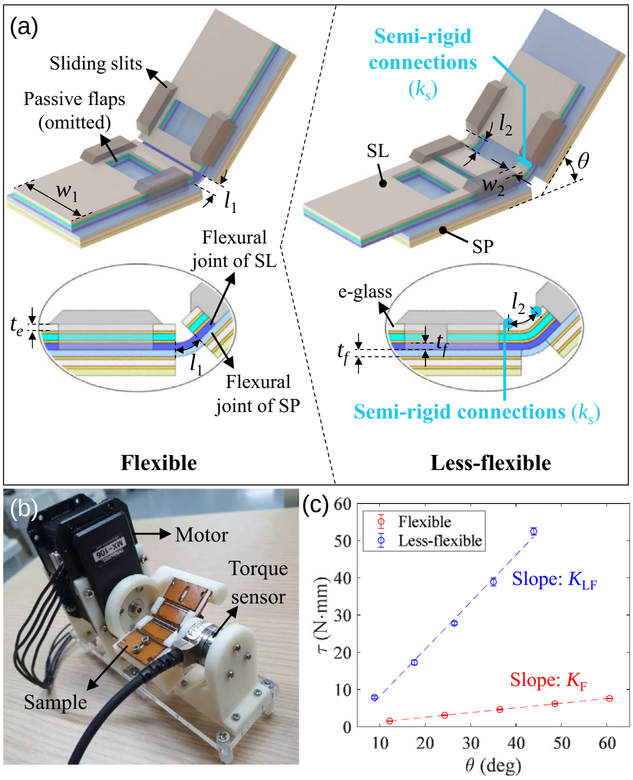

**Figure 4.** Stiffness change model of the flexural joint and its experimental setup. a): graphical illustration of a flexural joint in two stiffness states (left: F-state, right: LF-state). More detail explanations are given in the main text. b): experimental setup to measure the joint stiffness, c): a typical stiffness measurement result of the flexural joint.

**Table 1.** Young's moduli of materials used (A: adhesive).

| Marterials | Functionality | E [GPa] |
|---|---|---|
| 0.2 mm e-glass | Substrate layer of SL | 5.8 |
| 0.3 mm e-glass | | 8.3 |
| 0.4 mm e-glass | | 10.1 |
| 50 µm PET | Paddle-joint layer of SP and SL | 2.6 |
| 100 µm PET | | 2.3 |
| 50 µm A/PI/A tri-layer | Adhesive layer | 0.4 |
| 12.5 µm PI | Flap-joint layer | 3.0 |

prevent the bending of non-flexural-joint area of SP, its material property was not included in the model. The Young's moduli were experimentally measured by performing tensile test using an universal testing system (Instron 6800 series)[47] according to ASTM D882 guideline.[48]

### Flexible State

The two flexural joints were faced each other in F-state, and their thickness ($t_f$), width ($w_1$), and length ($l_1$) were the same. Also, the Young's modulus of the flexural joint was denoted as $E_1$ ($E$ of PET materials in Table 1). By assuming only these two flexural joints are deformed in F-state upon an external force, each flexural joint was modeled as a torsional spring with a spring constant $K_1$ as below [49]

$$K_1 = \frac{E_1 I_1}{l_1} \tag{1}$$

where $I_1 = w_1 t_f^3/12$ was the moment of inertia of a flexural joint. The resultant joint stiffness was simply modeled as two torsional springs connected in parallel

$$K_F = 2K_1 = \frac{E_1 w_1 t_f^3}{6 l_1} \tag{2}$$

To validate this model, a test bed shown in Figure 4b was implemented. A flexural joint sample was prepared by following the same fabrication method (refer Figure 2). The rotational axis of the sample was coaxially aligned with the center of a torque sensor (Nano 17)[50] and a motor (MAX-106)[51], which could bend the flexural joint in a certain angle $\theta$. The resultant torque $\tau$ was concurrently measured in 100 Hz using a USB-type data acquisition unit with LabVIEW software (National Instruments)[52]. When the flexural joint of each sample was bent to $\theta$ by the actuator, stabilized $\tau$ was measured. This was repeated five times for each $\theta$, and the samples in LF state were also tested in the same way. Typical measurement result is given in Figure 4c. The slope ($K_F$) obtained by liner regression was considered as the joint stiffness of the sample. Note that the joint stiffness at LF-state ($K_{LF}$) was also obtained in the same manner, and the slope is noticeably higher than $K_F$ as expected. For better verification of the model, $K_F$ of the innermost joint ($w_1 = 21$ mm) and the outermost joint ($w_1 = 14.6$ mm) were measured as representative cases. In addition, two different joint thickness ($t_f = 50$, 100 µm) were also considered.

The stiffness estimation based on (2) is compared with the associated experiment result, which is depicted with black markers, in **Figure** 5a. Five joint samples were fabricated for each set of design parameters (i.e., the $w_1$ and $t_f$), and $K_F$ was measured five times for each sample. Root-mean-square error (RMSE) of $t_f = 50$ µm case and $t_f = 100$ µm case was 0.22 and 0.86N mm rad$^{-1}$, respectively. After taking into account all the RMSE (for all $w_1$ and $t_f$ considered), the average error was 14.48%. Using (2) can provide reasonable approximation of flexural joint stiffness in F-state.

### Less-Flexible State

Part of the non-flexural-joint area of SL is faced with the flexural joint of SP in LF-state (refer Figure 4a). This non-flexural-joint area of SL (i.e., multi-layered composite beam) between the two sliding slits has the length and width of $l_2$ and $w_2$, respectively. Although the sliding slit was designed to firmly hold the SL and SP together, there was a slight gap between them due to the fabrication error of a 3D-printed sliding slit; this error was caused by formation of a small bulge at the corner of sliding slit during 3D printing. Therefore, rigid connection at the boundary of the sliding slit and the SL cannot be assumed when the

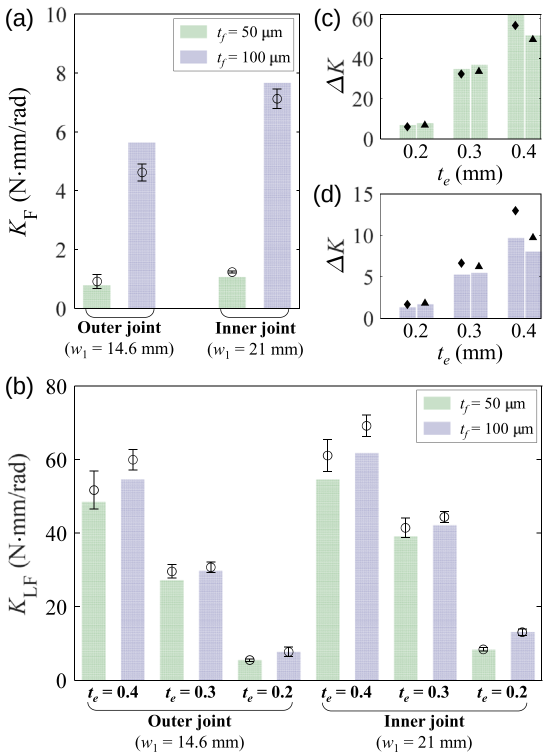

**Figure 5.** Comparison of theoretically calculated flexural joint stiffness ($K$) and experimentally measured values where $t_f$ is thickness of PET layer of SL and SP (outer joint: $w_1 = 14.6$ mm, inner joint: $w_1 = 21$ mm). a): flexible state, b): less-flexible state where $t_e$ is thickness of the e-glass in SL (refer Figure 4a), c) stiffness increased factor $\Delta K = K_{LF}/K_F$ when $t_f = 50\,\mu$m, (d) $\Delta K$ when $t_f = 100\,\mu$m. In c,d) the diamond markers and triangular markers indicate mean of $\Delta K$ from the outer and inner joints, respectively.

joint between these two sliding slits are bent. Instead, semi-rigid boundary condition was assumed by considering an imaginary torsional spring ($k_s$) at the material interface between the sliding slit and SL.[53] $k_s$ was experimentally found by measuring the required torque ($\tau_s$) to bend the composite beam between the two sliding slits by $\theta$, followed by solving the below equation in least-square manner[53]

$$\theta = \arctan\left(\frac{\tau_s l_2}{\mathrm{BS}} + \tan\frac{\tau_s}{k_s}\right) + \frac{\tau_s}{k_s} \tag{3}$$

where BS is bending stiffness of the composite beam. Note that the composite beam was a 5-layered laminate (refer Figure 2f), and its BS was obtained by following the multi-layered beam model.[54] Specifically, the sequence of thickness from paddle joint layer to substrate layer (refer Figure 2f) was denoted as $h_1, h_2, \ldots, h_5$. Also, the corresponding Young's modulus was defined as $E_1, E_2, \ldots, E_5$ in the same manner. Then $z_i$ was obtained from

$$z_i = \sum_{i=1}^{5} h_i. \tag{4}$$

After that, the distance from neutral axis of the composite beam and its bottom surface was calculated as

$$z_c = \frac{E_i W (z_i^2 - z_{i-1}^2)}{2(z_i - z_{i-1})} \tag{5}$$

where $z_0 = 0$ and $W = 2w_2$. Lastly, the BS was found

$$\mathrm{BS} = \sum_{i=1}^{5} \frac{E_i W((z_i - z_c)^3 - (z_{i-1} - z_c)^3)}{3} \tag{6}$$

By plugging (6) into (3), $k_s$ can be obtained where $\theta$ was controlled by the motor (refer Figure 4b). In the case of $\tau_s$ in (3), the total torque required to bend a LF-state sample ($\tau_{LF}$) by $\theta$ was measured using the same test bed. After that, a torque required to bend a single flexural joint layer of SP (i.e., $0.5\tau_F = 0.5K_F\theta$) was subtracted from $\tau_{LF}$; namely, $\tau_s = \tau_{LF} - 0.5\tau_F$. By bending a LF-state sample in multiple $\theta$, the resultant $k_s$ was obtained with different thickness of $t_e$ and $t_f$ as summarized in **Table 2**. Note that $k_s$ is different from the joint stiffness at LF-state, which is denoted as $K_{LF}$. As Young's moduli of e-glass were much higher than other materials (refer Table 1), e-glass thickness ($t_e$) was highly influential to $k_s$. Also, $k_s$ of the inner joint was higher than the one from outer joint at given $t_e$ and $t_f$ even though $w_2 = 2$ mm were the same for both inner and outer joints. This discrepancy could be attributed to the unmodeled effect of passive flaps as the inner joint had a wider passive flaps than outer joint. Finally, a semi-empirical estimation of the flexural joint stiffness in LF-state was

$$K_{LF} = 0.5K_F + \frac{\Delta\tau_s}{\Delta\theta} \tag{7}$$

where $\Delta\tau_s/\Delta\theta$ is the slope obtained in least-square manner from a $\tau_s$ versus $\theta$ graph; As $k_s$ in (3) is now known, the required $\tau_s$ to bend the SL composite in $\theta$ degrees can be calculated. $K_{LF}$ obtained from (7) was also compared with experimentally measured $K_{LF}$, and the result is given in Figure 5b. Just like F-state cases, $K_{LF}$ obtained from $t_f = 100\,\mu$m was greater than one from $t_f = 50\,\mu$m. $K_{LF}$ associated with the inner joint was also greater than its counterpart in outer joint as expected. The RMSE of $t_e = 0.2$, $t_e = 0.3$, and $t_e = 0.4$ mm was 0.4, 2.1, and 4.3N mm rad$^{-1}$, respectively when $t_f = 50\,\mu$m, which corresponds to 6.59% of error on average (by taking into account all the measurements without distinction of $t_e$ and $w_1$). When $t_f = 100\,\mu$m, the RMSE associated to $t_e = 0.2$, $t_e = 0.3$, and $t_e = 0.4$ mm was 1.05, 1.38, and 2.55N mm rad$^{-1}$, respectively. This corresponds to 6.19% of error on average.

The stiffness increased factor ($\Delta K = K_{LF}/K_F$) depicted in Figure 5c,d summarizes the accuracy of $\Delta K$ obtained from

**Table 2.** $k_s$ at semi-rigid connection area.

| | | $k_s$ (outer joint) | $k_s$ (inner joint) |
|---|---|---|---|
| $t_e = 0.4$ | $t_f = 50$ | $98.02 \pm 6.21$ | $110.50 \pm 4.77$ |
| | $t_f = 100$ | $105.23 \pm 4.16$ | $117.99 \pm 4.62$ |
| $t_e = 0.3$ | $t_f = 50$ | $54.82 \pm 2.15$ | $79.61 \pm 5.82$ |
| | $t_f = 100$ | $52.81 \pm 2.91$ | $78.32 \pm 2.14$ |
| $t_e = 0.2$ | $t_f = 50$ | $10.26 \pm 0.38$ | $15.93 \pm 0.63$ |
| | $t_f = 100$ | $9.84 \pm 1.92$ | $18.86 \pm 1.07$ |

(2) and (7) compared to experimentally measured results. Figure 5c,d corresponds to $t_f = 50\,\mu m$ and $t_f = 100\,\mu m$, respectively; while the diamond markers and triangular markers indicate experimentally measured $\Delta K$ from the outer and inner joint, respectively. For a given set of $t_e$ and $t_f$, $\Delta K$ of the innermost and outermost joints were still in the same order; and therefore, studying the stiffness change of these two representative joints can be considered as a reasonable approximation of the paddle stiffness change. Within the design parameters under considered, the largest $\Delta K$ was almost close to 60. As the $K_f$ associated to $t_f = 50\,\mu m$ was smaller than one from $t_f = 100\,\mu m$ (refer Figure 5a), the resultant $\Delta K$ obtained from $t_f = 50\,\mu m$ (Figure 5c) was noticeably larger than $t_f = 100\,\mu m$ case (Figure 5d). Overall, the model-driven $\Delta K$ was reasonably accurate; however, due to the accumulated error of $K_{LF}$ and $K_F$ when $t_f = 100\,\mu m$ and $t_e = 0.4\,mm$, the resultant $\Delta K$ exhibited particularly large error compared other cases. As letting $t_f = 50\,\mu m$ could achieve larger stiffness change, $t_f$ was fixed to $50\,\mu m$ in rest of the sections.

## 3. Analysis of the Proposed Paddle

### 3.1. Hydromechanical Bending Behaviors

To better observe and characterize the hydromechanical aspects of the proposed paddle, a test bed shown in **Figure 6**a was built. The entire test bed was firmly fixed to the force/torque sensor (ATI Nano 17)[50] where the rotational axis of the paddle and the center of the sensor were coaxially aligned. The paddle was driven by a waterproof servo motor (HS-5086WP),[55] which was completely submerged in underwater. To monitor the position and driving speed of the proposed paddle during operation, a magnetic encoder (EzEncoder, i2A Systems)[56] was installed between the force/torque sensor and the motor where a small magnet was attached at the tip of the rotational axis. The resolution of magnetic encoder was 12 bit, and it was calibrated to sense a targeted ROM. The thrust data obtained from the force/torque sensor was measured in 200 Hz using a USB-type data acquisition unit and LabVIEW software (National Instruments).[52] Thrust measurement was post-processed with a low pass filter with 6 Hz of cutoff frequency to remove noise.

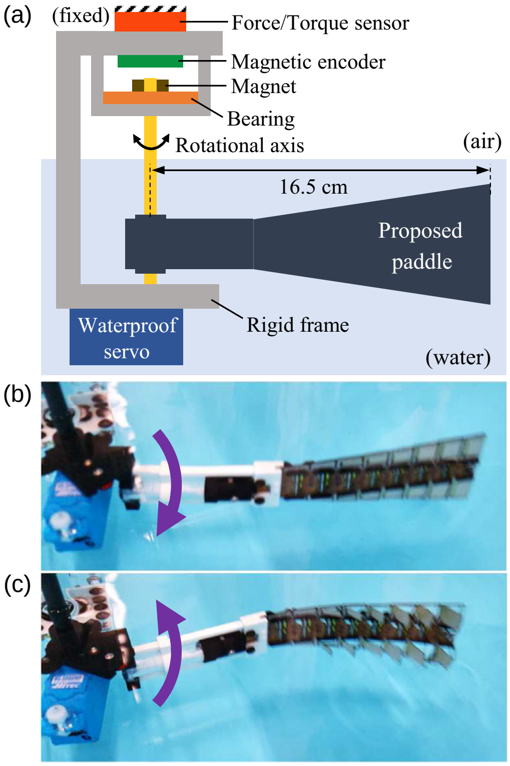

**Figure 6.** A test bed for characterization of the proposed swimming paddle. a): Illustration of the test bed, b): snapshot of the swimming paddle in underwater driven by the motor during power stroke, c): the passive flaps are opened during recovery stroke for drag reduction.

The motor installed on the test bed was programmed to drive the paddle in a predefined speed to observe the bending behavior as shown in Figure 6b,c. During the power stroke (refer Figure 6b), all the passive flaps were closed to maximize thrust. On the other hand, the flaps were passively opened during recovery stroke to reduce drag force (refer Figure 6c).

Morphological difference of the paddle in F-state and LF-state was much clear when its underwater actuation was observed from the top view as shown in **Figure 7** where range of motion ($R$) was 90°. Note that the paddle was driven in counterclockwise and clockwise direction during recovery stroke and power stroke, respectively. The flexural joints were all bent rearward during recovery stroke, which also attributed reduction of hydro-drag force. Especially, the degree of bending was noticeably larger when the paddle was in F-state (refer Figure 7a2). This large bending angle was beneficial in reducing unwanted drag force; however, it also required prolong time to fully unfold the flexural joints during power stroke. As partially unfolded paddle could generate only smaller thrust than a fully-unfolded paddle, the advantage of large flexural joint bending during recovery stroke became a performance-degrading factor during power stroke. Note that all the flexural joints were fully unfolded in the middle phase of power stroke. On the other hand, LF-state paddle was characterized by small flexural joint bending during recovery stroke as shown in Figure 7b2, which imposed large drag. This small bending angle, however, enabled quick joint unfolding and maintained a straight paddle at the beginning of power stroke. This passive folding and unfolding of flexural joints are eventually depending on their stiffness and actuation frequency. More details will be discussed in Section 4.

### 3.2. Hydrodynamic Thrust and Efficiency

Thrust ($T$) generated from three sets of paddles (i.e., $t_e = 0.2, 0.3, 0.4\,mm$) were measured by varying $R$, driving frequency ($f$), and stiffness. As $T$ was time varying value during propulsion, time-averaged thrust ($T_a$) was calculated by repetitively driving the paddle 15 cycles underwater to compare $T_a$, which is defined as

$$T_a = \frac{\int_0^t T(t)\mathrm{d}t}{t} \tag{8}$$

where $t$ is time. To better characterize how $T_a$ was changed by simply switching the stiffness state, thrust amplified ratio ($\Delta T_a$) was also considered

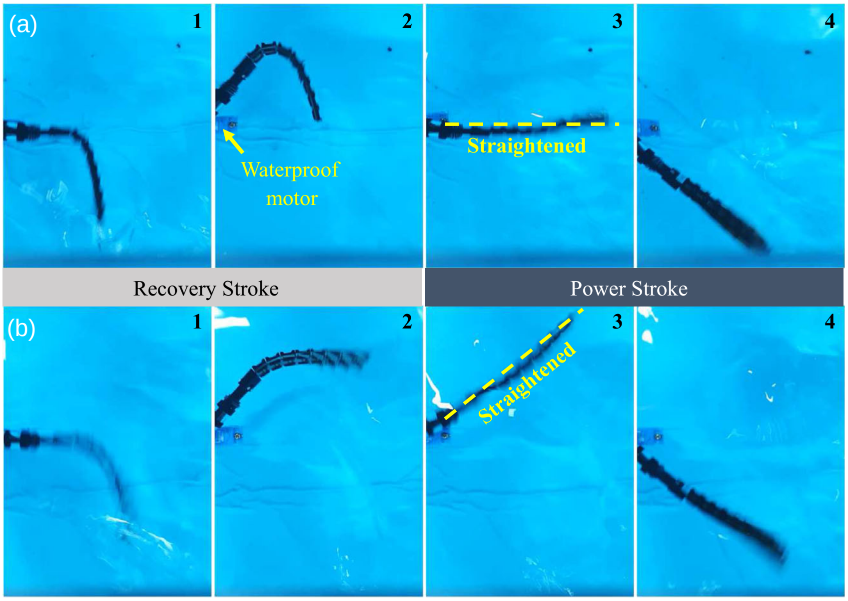

**Figure 7.** Bending behavior of the paddle observed from top view when range of the motion ($R$) was 90° (1-2: recovery stroke, 3-4: power stroke). a): selected footage of the paddle in F-state, b): selected footage of the paddle in LF-state.

$$\Delta T_a = \frac{T_{a,LF} - T_{a,F}}{T_{a,F}} \tag{9}$$

where $T_{a,F}$ and $T_{a,LF}$ was $T_a$ in F-state and LF-state, respectively. The paddle connected to the motor can physically rotate up to 100°; however, to avoid any damage caused by repetitive contact between the paddle and the motor, maximum $R$ was set to 90°. Also, to study a broader range of actuation frequency, two additional $R$ smaller than 90° were considered; namely, 50° and 70°. Due to the actuation speed limitation of the waterproof motor, which was $110 - 120^\circ\,s^{-1}$, the highest drivable $f$ was set to 2.2, 1.7, and 1.3 Hz for 50°, 70°, and 90° of $R$, respectively. Note that multiplying each $f$ with the associated ROM yields an angular speed, which is still within the speed limit of the motor. All the measurement results are depicted in **Figure 8** where face-filled circular markers indicate $T_{a,LF}$ in Figure 8a–c. As observed from previous related research, $T_a$ exhibited positive correlations with $f$ and $R$.[4,5] Overall, $T_{a,F}$ was larger than $T_{a,LF}$ when $f$ was smaller than 1 Hz and vice versa at $f$ higher than 1 Hz. This tendency is much clearly observed from Figure 8d–f; note that negative $\Delta T_a$ indicates that $T_a$ was greater in F-state than the associated LF-state. However, $\Delta T_a$ became positive as $f$ was higher than 1 Hz. These tendencies were observed from all the three $t_e$ values, which showed that increasing the paddle stiffness at higher $f$ (i.e., 1 Hz in this work) was beneficial to generate large thrust. Similar results were also reported from other drag-based propulsors.[8,10,14] Although $T_a$ obtained from $R = 50^\circ$ cases were comparatively low, the associated $\Delta T_a$ was particularly large. This result was especially noticeable when $t_e = 0.4$ mm as the stiffness change was the greatest at thicker $t_e$. As LF-state paddle was characterized by quick shape restoration at the beginning of power stroke (refer Figure 7b), this property became more advantageous to generate large thrust as $R$ became smaller. When $R$ was larger than 50°, a F-state paddle had more time to restore its shape back to straight posture, and the resultant $\Delta T_a$ was small.

## 4. Swimming Performance Verification

### 4.1. Implementation of the Robot

One pair of the proposed paddles was employed to a non-tethered swimming robot shown in **Figure 9**a. Each paddle was individually driven by the same waterproof servo motor (HS-5086WP).[55] Cross section of the hull was adapted from an airfoil (Eppler 863)[57] to reduce the hydrodynamic drag during swimming. The hull was split into 2 parts as shown in Figure S3, Supporting Information, to store electronics inside. The hull was 3D printed and brushed with water-protective coating (XTC-3D, Smooth-On)[58] to prevent water intrusion inside the hull. Two waterproof servo motors were fixed to each side of the hull using bolts and nuts. All the electronics (refer Figure 9b) were contained inside the hull including a 11.1 V Li-Po battery, a Teensy 4.0 board for the motor control, a Bluetooth chip for remote communication (e.g., wireless transmission of measured electric current data), and voltage converters for the motors and the Teensy board. Before assembling the 2 pieces of hulls, a vacuum grease was applied alongside the edge of the hull for watertight sealing. Though it is not shown in Figure 9a, two motion capture markers were installed at the designated site (refer Figure S3, Supporting Information) by connecting the markers and the body frame with 5 cm long carbon rods to avoid direct water contact to the markers. The longitudinal body length and total mass of the robot was 15.2 cm and 414 gram, respectively.

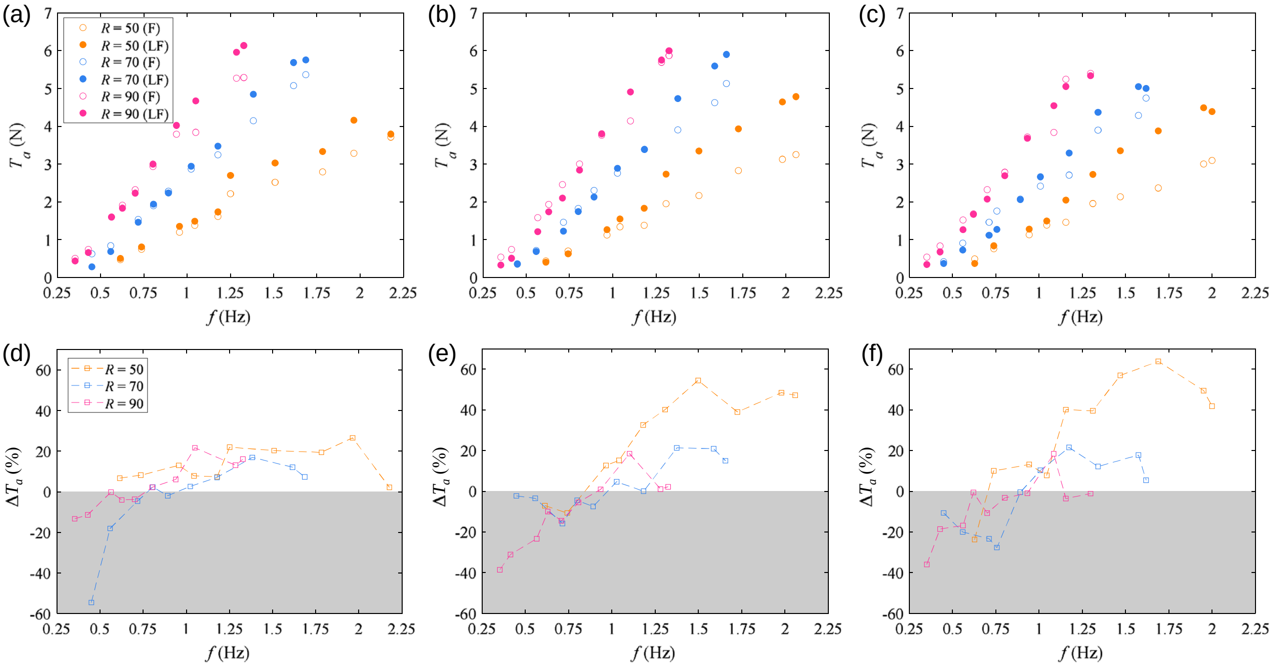

Figure 8. Time-averaged thrust ($T_a$) and thrust-amplified ratio ($\Delta T_a$) obtained from the proposed paddle by varying range of motion ($R$), flexural joint stiffness, and actuation frequency ($f$). a,d): when $t_e = 0.2$ mm, b,e): when $t_e = 0.3$ mm, c,f): when $t_e = 0.4$ mm.

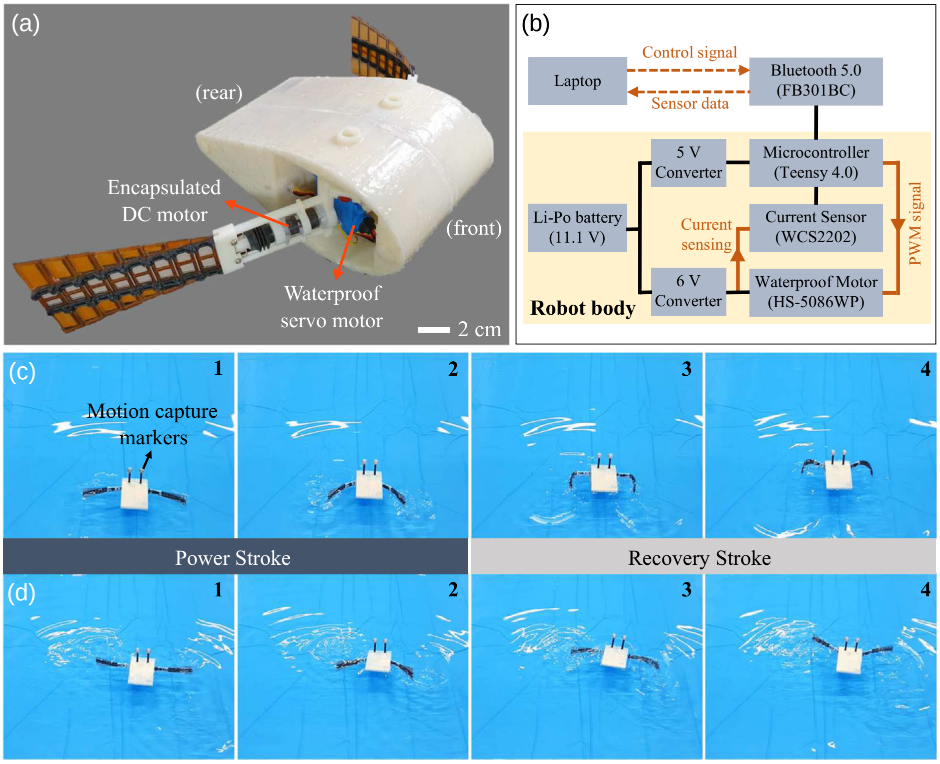

Figure 9. Implemented swimming robot propelled by the proposed paddles and its swimming motion. a): the proposed non-tethered swimming robot, b): hardware configuration inside the robot body, c,d): swimming motion of the robot using F and LF-state paddles where 2 motion capture markers were attached at the robot for motion tracking (c: F-state, d: LF-state).

### 4.2. Swimming Experiment

The robot was tested inside a $2 \times 3\,\text{m}^2$ sized water tank surrounded by 8 motion capture cameras (Prime 13, Optitrack).[59] The robot additionally had two motion capture markers as shown in Figure 9c for position tracking. A supporting media that shows swimming of the robot is available; Video S2, Supporting Information. Positional data of the robot was acquired at 120 Hz rate using Motive software.[60] Due to the water splash caused by the swimming, the markers were sometimes not sensed by the motion capture cameras during the fractions of second. This missing data was filled by cubic spline using an internal tool provided by Motive software. All the positional data were post-processed by a low pass filter with 6 Hz of cutoff frequency to remove noise. During the swimming, power consumption of the robot was collected via Bluetooth connection at 60 Hz rate to obtain an average power consumption ($P$). By adjusting $f$, $R$, $t_e$, and stiffness state, the average swimming velocity ($V_a$) of the robot and the associated cost of transport ($\text{COT} = P/mgV_a$) were measured where $m$ and $g$ was mass of the robot and gravitational acceleration, respectively. All these results are depicted in **Figure 10**. As the maximal $f$ at $R = 90°$ was smaller than that of $R = 70°$ or $R = 50°$ (refer Figure 8), $R$ was decreased from 90° to 50° as $f$ was increased to run the experiment at wider range of $f$. Thus, the result associated to $R = 90°$, 70°, and 50° was highlighted with red, blue and yellow background color, respectively. In the case of $V_a$ and COT obtained from $0.25 < f < 1.3$ Hz associated with $R = 50, 70°$, both $V_a$ and $COT$ were generally proportional to $f$; however, the $V_a$ was generally smaller than that of $R = 90°$ when $0.25 < f < 1.3$ Hz. Since maintaining large $R$ ensured higher thrust, we kept $R = 90°$ whenever it was feasible, but gradually reduced $R$ to demonstrate swimming with higher $f$, beyond the maximally attainable $f$ with $R = 90°$.

As expected from the thrust measurement result, the fastest $V_a$ was achieved when $R = 90°$ regardless of $t_e$, especially in LF-state. Given that $R = 90°$, the positive correlation between $V_a$ and $f$ was especially noticeable. A similar relation was reported not only from a pectoral fin-propelled fish robot,[10] but also from the kinematic study of a fish.[61] Even though $V_a$ was decreased in smaller $R$, the associated COT was kept increasing due to the high energy expenditure to maintain fast beating of the paddles. This trend was similar to a simulated COT of anguilliform fish;[61] COT was more prone to increase upon increasing of tail-beat frequency rather than amplitude. Overall, $V_a$ measured in LF-state was either almost the same or faster than its counterpart in F-state for all $t_e$ considered. However, it does not mean that LF-state was always energy efficient. For example, there was a clear threshold $f$ (around 0.75 Hz) where COT associated to LF-state was greater than that of F-state in Figure 10a. Although $t_e = 0.2$ mm case exhibited that $V_a$ obtained from LF-state was faster than F-state in all $f$ considered, the robot had to spend more power when $f$ was lower than 0.75 Hz. By considering that the difference of $V_a$ in F and LF-states was fairly small when $f < 0.75$ Hz (Figure 10a), maintaining F-state was beneficial during slow swimming. However, switching the paddle stiffness to LF was advantageous for fast swimming with reduced COT when $f$ was equal to or higher than 0.75 Hz. It is generally well-known that there is no a unique stiffness that can maximize swimming efficiency in all condition.[9] Rather than swimming with a fixed stiffness propulsor, having a stiffness-tunable ability is beneficial, especially for a hight-frequency swimming robot.[31] As an example, a fish robot driven by a passive tail (consists of two spring steels as flexural joints and rigid plates)

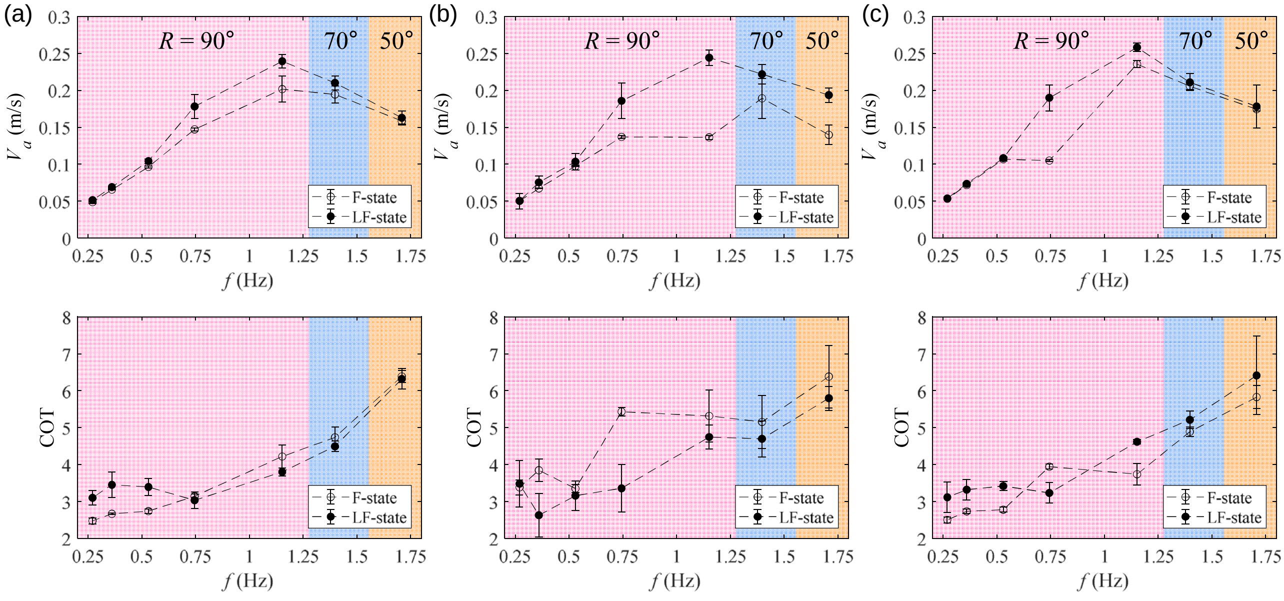

**Figure 10.** Averaged swimming velocity ($V_a$, top) and the associated cost of transport (COT, bottom) of the proposed robot during swimming at different beating frequencies ($f$), range of motion ($R$), and stiffness state (a: $t_e = 0.2$ mm, b: $t_e = 0.3$ mm, c: $t_e = 0.4$ mm). Note that $R$ was decreased from 90° to 50° to test the robot at wider range of $f$ (red area: $R = 90°$, blue area: $R = 70°$, yellow area: $R = 50°$).

required a large tail stiffness when swimming with a higher frequency for better performance.[15] Despite the morphological difference between a bilateral paddle-driven rowing robot (including our robot) and tail fin-driven fish robot, a positive correlation between the propulsor stiffness and driving frequency for improved swimming performance was valid for both robots.

Unlike the COT tendency in Figure 10a, maintaining LF-state was always beneficial by considering the resultant low COT and fast $V_a$ in all the range of $f$ when $t_e = 0.3\,\text{mm}$ (refer Figure 10b). On the other hand, COT in LF-state was higher than that of F-state (except when $f = 0.75\,\text{mm}$) when $t_e = 0.4\,\text{mm}$ (refer Figure 10c). Despite the large stiffness difference in LF-state from $t_e = 0.2$ to $0.4\,\text{mm}$ (refer Figure 5c), the resultant $V_a$ (in LF-state) was not much that different. As reported in ref. [11], multiple stiffness distributions in a robotic tail can yield an identical swimming speed. Similarly, rowing paddles with different stiffness could propel the robot in almost the same speed, but more study is required to identify an exact reason. The bottom line was that the stiffness adjustment of the proposed paddle was meaningful and lead to COT reduction depending on $f$ only when $t_e$ was 0.2 mm. Therefore, stiffness adjustment mechanism could be unnecessary as $t_e$ became thicker. It was suggested that a small or slowly actuated tail fin can be a near-optimal even without tunable stiffness.[31] Therefore, it is expected that the proposed paddle with $t_e = 0.3$ and 0.4 mm need to be scaled up or actuated with much higher frequency to make the stiffness-adjustable mechanism facilitates noticeable swimming behavior change.

### 4.3. Discussion

For comprehensive swimming experiment, each paddle was driven in 5 different $f$ for a given stiffness state in 3 different $R$ (i.e., $50°, 70°, 90°$) to measure $V_a$ and COT. In Figure 10, some of $V_a$ and COT were not deliberately shown for a given $R$; for example, $V_a$ and COT associated with $R = 90°$ was not depicted when $f > 1.25\,\text{Hz}$, as $V_a$ was slower (or, COT was higher) than one from $R = 50°$ or $R = 70°$. These non-depicted data were all included in **Figure 11** by calculating the percentage of $V_a$ change ($\Delta V_a$) and the associated COT change ($\Delta$COT) when the paddle stiffness was switched from F to LF-state at a given $f$, $R$, and $t_e$. More specifically, $\Delta V_a$ and $\Delta$COT were defined as

$$\Delta V_a = \frac{V_{a,\text{LF}} - V_{a,\text{F}}}{V_{a,\text{F}}} \times 100\% \tag{10}$$

$$\Delta\text{COT} = \frac{\text{COT}_{\text{LF}} - \text{COT}_{\text{F}}}{\text{COT}_{\text{F}}} \times 100\% \tag{11}$$

where the subscript F and LF stands for the result associated with the F-state and LF-state paddle. The data obtained from different $t_e$ was expressed with different shapes of markers; $t_e = 0.2$, 0.3, and 0.4 mm corresponded to asterisk, triangle, and diamond marker, respectively. In addition, $\Delta V_a$ and $\Delta$COT obtained from $f$ higher than 1.25 Hz were highlighted with face-filled markers. To distinguish different $R$, magenta, blue, and orange color was assigned to the markers that correspond to $R = 90°$, $70°$, and $50°$, respectively.

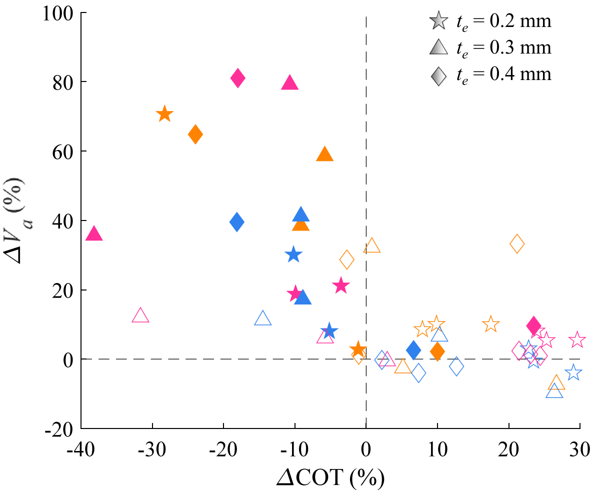

**Figure 11.** The percentage of $V_a$ change ($\Delta V_a$) and the associated COT change ($\Delta$COT) by switching the paddle stiffness from F to LF-state. The result obtained from $f > 1.25\,\text{Hz}$ cases were depicted with face-filled markers, while the rest of them (i.e., $f < 1.25\,\text{Hz}$) were expressed with hollow markers. Magenta, blue, and orange colored markers correspond to $R = 90°$, $70°$, and $50°$, respectively.

All the face-filled markers were located in the region of $\Delta V_a > 0$, which indicates that increasing the stiffness at higher beating frequency (in this work: $f > 1.25\,\text{Hz}$) increased the swimming speed of the robot. In particular, most of the face-filled markers were located in $\Delta\text{COT} < 0$ region; these include all the markers associated to $t_e = 0.2$ and 0.3 mm, and only some of 0.4 mm. As a result, switching the paddle stiffness to LF-state not only increased swimming speed, but also reduced the resultant COT in most cases unless $t_e$ was unnecessarily thick. Thus, it is encouraged to test slightly elevated stiffness at first (with fixed $R$ and $f$) and gradually increase the stiffness until an optimal stiffness is found in future study of swimming robot. In this study, letting $t_e = 0.2\,\text{mm}$ was already enough to demonstrate the usefulness of a variable stiffness paddle. According to Figure 5c, this corresponded to the stiffness change factor of around 5. Therefore, a variable stiffness mechanism intended to achieve improved swimming does not necessarily need to have an overly large range of stiffness change. In addition, a more continuous way of adjusting the paddle stiffness would be beneficial for better stiffness optimization. Sliding laminate-based mechanism was already proven its capability of continuous stiffness change depending on the displacement of sliding laminate.[24] Thus, the proposed paddle is also expected to have the same ability with little design modification.

As multiple parameters (e.g., $R$, $f$, stiffness) can result in the same $V_a$, it is better to maintain large $R$ if possible to reduce resultant COT. Suppose the robot has a target $V_a = 0.17\,\text{m}\,\text{s}^{-1}$. From Figure 10, multiple set of parameters can reach the same $V_a$; for example, both ($R = 90°$, $f = 0.75\,\text{Hz}$, $t_e = 0.2\,\text{mm}$, LF − state) and ($R = 50°$, $f = 1.7\,\text{Hz}$, $t_e = 0.4\,\text{mm}$, LF − state) resulted in $V_a$ close to $0.17\,\text{m}\,\text{s}^{-1}$. Apparently, the former parameter set required much less COT than the latter set.

It was experimentally demonstrated that maintaining flexible stiffness was beneficial for the robot when swimming with lower

$f$ (refer Figure 10a). According to our previous work,[8] introducing a short relaxation time (i.e., a moment when no actuation is performed to passively restore flexural joints before executing next power stroke) could increase thrust generated from a swimming leg with passive joints. In Figure 7a, the flexural joints were bent in posterior side after finishing the recovery stroke. Here, introducing a short relaxation time can restore those deformed joints to re-extended posture (just like the straightened shape shown in footage 3 of Figure 7a) before starting a next power stroke. Since the proposed paddle is essentially a drag-powered swimming appendage with passive joints just like the passive swimming leg in ref. [8], introducing a relaxation time is expected to improve the thrust generated by the paddle in F-state. In other words, not only reducing the paddle stiffness but also introducing a short relaxation time can further increase thrust when the robot is swimming with lower $f$.

## 5. Conclusion and Future Work

This work proposed a new articulated swimming paddle, which can adjust its stiffness (i.e., F and LF-states) by simply displacing a thin laminate inside. Owing to the passively driven articulated joints and flaps, the paddle can generate thrust by simple repetitive actuation of a waterproof motor. The range of stiffness change was tunable depending on the thickness of sliding laminate; the largest stiffness increased ratio shown in this study was 60. A semi-empirical model, which can estimate the stiffness change, was also proposed and exhibited reasonable model accuracy in change of multiple design parameters. It was found from thrust measurement that, the paddle in LF-state could generate higher thrust than F-state when beating frequency ($f$) was higher than about 1 Hz; vice versa when $f$ was smaller than 1 Hz. This thrust amplification was even more noticeable as the range of motion became smaller with a thicker sliding laminate. The paddles were also applied to a non-tethered swimming robot and the resultant locomotion was comprehensively studied in terms of swimming speed and cost of transport. When the robot was swimming in a $f$ higher than certain threshold, increasing the paddle stiffness resulted in faster swimming with reduced cost of transport. However, this locomotory beneficial effect acquired by the stiffness change was hardly observed as the thickness of sliding laminate became thicker. Therefore, the dimensions of sliding laminate (e.g., width, thickness) has to be carefully selected to achieve improved swimming performance when the robot is driven by varying beating frequencies.

As future work, the paddle stiffness needs to be more continuously adjustable for better stiffness optimization. It was discussed in previous section that gradually increasing the paddle stiffness would be much helpful to identify an optimal stiffness for a given $R$ and $f$. Secondly, optimal stiffness distribution of the flexural joints along the paddle length is worth to be investigated to attain maximal thrust. In ref. [7], a trapezoidal fin with stiffer at inner (proximal) joint and softer at outer (distal) joint could attain maximal thrust. Although, the inner joint of the proposed paddle already has a larger width than the outer joint (refer Figure 3), the stiffness distribution of all the 8 flexural joints was not optimized yet. Lastly, demonstrating an online stiffness adjustment of the robot would much enlarge its practical applications. Currently, the paddle stiffness must be changed by a human operator by monitoring the swimming speed. Toward more autonomous operation, embedding an accelerometer to the robot can be considered to dynamically sense swimming speed and adjust the paddle stiffness according to a suitable policy.

## Supporting Information

Supporting Information is available from the Wiley Online Library or from the author.

## Acknowledgements

The authors are grateful for the technical help provided by Junhyeok Cha during the early prototyping of the stiffness-adjustable paddle. They also wish to thank Minwoong Jo and Sihyeon Kim for their help in swimming experiment of the robot. This work was supported by the National Research Foundation of Korea (NRF) Grant funded by the Korean Government (MSIT) (No. NRF-2019R1A2C2084677).

## Conflict of Interest

The authors declare no conflict of interest.

## Data Availability Statement

All data are reported in the manuscript.

## Keywords

drag-based swimming, flexural joint, swimming paddle, swimming robot, variable stiffness

Received: October 11, 2022
Revised: December 17, 2022

[1] K. N. Lucas, N. Johnson, W. T. Beaulieu, E. Cathcart, G. Tirrell, S. P. Colin, B. J. Gemmell, J. O. Dabiri, J. H. Costello, *Nat. Commun.* **2014**, *5*, 3293.
[2] P. Deshpande, A. Vishwasrao, *J. Fluid Mech.* **2021**, *922*, A13.
[3] X. Bai, Y. Wang, R. Wang, S. Wang, M. Tan, *IEEE/ASME Trans. Mechatron.* **2021**, *27*, 868.
[4] D. B. Quinn, G. V. Lauder, A. J. Smits, *J. Fluid Mech.* **2014**, *738*, 250.
[5] P. A. Dewey, B. M. Boschitsch, K. W. Moored, H. A. Stone, A. J. Smits, *J. Fluid Mech.* **2013**, *732*, 29.
[6] F. Paraz, L. Schouveiler, C. Eloy, *Phys. Fluids* **2016**, *28*, 011903.
[7] S. R. N, S. Sen, C. Har, *Mech. Mach. Theory* **2018**, *129*, 218.
[8] B. Kwak, D. Lee, J. Bae, *Bioinspiration Biomimetics* **2019**, *14*, 066003.
[9] D. Quinn, G. Lauder, *Bioinspiration Biomimetics* **2022**, *17*, 011002.
[10] S. B. Behbahani, X. Tan, *J. Nonlinear Sci.* **2017**, *27*, 1155.
[11] B. Chen, H. Jiang, *IEEE Trans. Rob.* **2021**, *37*, 1712.
[12] S. Kobayashi, T. Ozaki, M. Nakabayashi, H. Morikawa, A. Itoh, in *IEEE Inter. Conf. on Robotics and Biomimetics*, IEEE, Kunming, China **2006**, pp. 463–467.
[13] S. Kobayashi, M. Nakabayashi, H. Morikawa, *J. Biomech. Sci. Eng.* **2006**, *1*, 280.

[14] S. Kobayashi, H. Morikawa, H. Soyano, M. Nakabayashi, *Int. J. Offshore Polar Eng.* **2013**, *23*, 172.
[15] B. Lu, C. Zhou, J. Wang, Y. Fu, L. Cheng, M. Tan, *IEEE Rob. Autom. Lett.* **2022**, *7*, 834.
[16] Y.-J. Park, T. M. Huh, D. Park, K.-J. Cho, *Bioinspiration Biomimetics* **2014**, *9*, 036002.
[17] Y.-J. Park, *J. Korea Acad.-Ind. coop. Soc.* **2020**, *21*, 103.
[18] M. Ziegler, M. Hoffmann, J. P. Carbajal, R. Pfeifer, in *IEEE Inter. Conf. on Robotics and Automation*, IEEE, Shanghai, China **2011**, pp. 2705–2712.
[19] B. Zhong, S. Zhang, M. Xu, Y. Zhou, T. Fang, W. Li, *IEEE/ASME Trans. Mechatron.* **2018**, *23*, 542.
[20] M. Ziegler, R. Pfeifer, in *Sensory Feedback of a Fish Robot With Tunable Elastic Tail Fin. From Biomimetic and Biohybrid Systems. Living Machines* (Eds: N. F. Lepora, A. Mura, H. G. Krapp, P. F. M. J. Verschure, T. J. Prescott), Springer, Berlin, Heidelberg **2013**.
[21] M. Sharifzadeh, Y. Jiang, D. M. Aukes, *IEEE Rob. Autom. Lett.* **2021**, *6* 3437.
[22] M. Sharifzadeh, D. M. Aukes, *IEEE/ASME Trans. Mechatron.* **2021**, *26* 503.
[23] M. Jiang, Q. Yu, N. Gravish, in *IEEE Inter. Conf. on Soft Robotics (RoboSoft)*, IEEE, Yale University, CT **2021**, pp. 315–320.
[24] M. Jiang, N. Gravish, *Smart Mater. Struct.* **2021**, *30*, 035005.
[25] H. Kim, J. Lee, *Ocean Eng.* **2017**, *130*, 310.
[26] S. B. A. Kashem, S. Jawed, J. Ahmed, U. Qidwai, *Robotics* **2019**, *8*, 77.
[27] X. Jia, Z. Chen, A. Riedel, T. Si, W. R. Hamel, M. Zhang, *IEEE Trans. Rob.* **2015**, *31*, 1432.
[28] Y. Chen, N. Doshi, B. Goldberg, H. Wang, R. J. Wood, *Nat. Commun.* **2018**, *9*, 2495.
[29] A. Simha, R. Gkliva, Ü. Kotta, M. Kruusmaa, *IEEE Rob. Autom. Lett.* **2020**, *5*, 3176.
[30] V. A. Pham, T. T. Nguyen, B. R. Lee, T. Q. Vo, *Robotica* **2020**, *38*, 699.
[31] Q. Zhong, J. Zhu, F. E. Fish, S. J. Kerr, A. M. Downs, H. Bart-Smith, D. B. Quinn, *Sci. Rob.* **2021**, *6*, eabe4088.
[32] Y.-J. Park, J.-G. Lee, S. Jeon, H. Ahn, J. Koh, J. Ryu, M. Cho, K.-J. Cho, *J. Intell. Mater. Syst. Struct.* **2016**, *27*, 995.
[33] M. Manti, V. Cacucciolo, M. Cianchetti, *IEEE Rob. Autom. Mag.* **2016**, *23*, 93.
[34] S. B. Behbahani, X. Tan, *Smart Mater. Struct.* **2017**, *26*, 085014.
[35] H. Imamura, K. Kadooka, M. Taya, *Soft Matter* **2017**, *13*, 3440.
[36] M. Henke, J. Sorber, G. Gerlach, *Adv. Sci. Technol.* **2013**, *79*, 75.
[37] O. Tabata, S. Konishi, P. Cusin, Y. Ito, F. Kawai, S. Hirai, S. Kawamura, *Sens. Actuators, A* **2001**, *89*, 119.
[38] B.-K. Song, J.-Y. Yoon, S.-W. Hong, S.-B. Choi, *Materials* **2020**, *13*, 953.
[39] B. E. Schubert, D. Floreano, *RSC Adv.* **2013**, *3*, 24671.
[40] A. Firouzeh, J. Paik, *IEEE/ASME Trans. Mechatron.* **2017**, *22*, 2165.
[41] W. Shan, S. Diller, A. Tutcuoglu, C. Majidi, *Smart Mater. Struct.* **2015**, *24*, 065001.
[42] M. Henke, G. Gerlach, *J. Intell. Mater. Syst. Struct.* **2016**, *27*, 375.
[43] M. B. Oliveira, C. Liu, M. Zhao, S. M. Felton, in *ASME Conf. on Smart Materials, Adaptive Structures and Intelligent Systems*, San Antonio, TX, USA **2018**, pp. 8, SMASIS2018–8049, V002T08A009.
[44] I. Ribera, G. N. Foster, *Biol. J. Linn. Soc.* **1997**, *61*, 537.
[45] J. Lee, Y.-J. Park, K.-J. Cho, D. Kim, H.-Y. Kim, *J. Fluids Struct.* **2017**, *71*, 70.
[46] F. Zuliani, J. Paik, *Smart Mater. Struct.* **2022**, *31*, 115023.
[47] 6800 series, Instron [Online], https://www.instron.com/ (accessed: October 2022).
[48] *Standard Test Method for Tensile Properties of Thin Plastic Sheeting*, ASTM **2018**, 12, https://doi.org/10.1520/D0882-18.
[49] L. L. Howell, *Compliant Mechanisms*, Wiley, New York **2001**.
[50] Nano 17, Ati Industrial Automation [Online], http://www.ati-ia.com/ (accessed: October 2022).
[51] MAX 106, Dynamixel [Online], https://www.robotis.us/dynamixel/ (accessed: October 2022).
[52] National Instruments, LabVIEW [Online], https://www.ni.com/ (accessed: October 2022).
[53] H. Zhang, H. Feng, J.-L. Huang, J. Paik, *Extreme Mech. Lett.* **2021**, *45*, 101213.
[54] Z.-F. Zhou, M.-Z. Meng, C. Sun, Q.-A. Huang, *Micromachines* **2019**, *10*, 669.
[55] HS-5086WP, Hitec [Online], https://www.hitecrcd.com (accessed: October 2022).
[56] E, i2a Systems [Online], https://i2asys.com (accessed: October 2022).
[57] EPPLER 863 STRUT AIRFOIL Airfoil tools [Online], http://airfoiltools.com/ (accessed: December 2021).
[58] Smooth-On, Xtc-3d [Online], https://www.smooth-on.com (accessed: October 2022).
[59] OptiTrack, Prime 13 [Online], https://optitrack.com (accessed: October 2022).
[60] OptiTrack, Motive, [Online], https://optitrack.com (accessed: October 2022).
[61] G. Li, H. Liu, U. K. Müller, C. J. Voesenek, J. L. van Leeuwen, *Proc. R. Soc. B* **2021**, *288*, 1.